DNS of a spatially evolving hypersonic turbulent boundary layer at Mach 8

LIANG Xian[*] & LI XinLiang

Laboratory of High Temperature Gas Dynamics, Institute of Mechanics, Chinese Academy of Sciences, Beijing 100190, China

This paper reports the direct numerical simulation (DNS) for hypersonic turbulent boundary layer over a flat-plate at Ma_∞=8 with the ratio of wall-to-freestream temperature equal to 1.9, which indicates an extremely cold wall condition. It is primarily used to assess the wall temperature effects on the mean velocity profile, Walz equation, turbulent intensity, strong Reynolds analogy (SRA), and compressibility. The present high Mach number with cold wall condition induces strong compressibility effects. As a result, the Morkovin's hypothesis is not fully valid and so the classical SRA is also not fully consistent. However, some modified SRA is still valid at the far-wall region. It is also verified that the semi-local wall coordinate y^* is better than conventional y^+ in analysis of statistics features in turbulent boundary layer (TBL) in hypersonic flow.

1 Introduction

All, or most, of the supersonic aircraft boundary layers are compressible turbulence. Friction resistance and heat flux along the outside metallic layer (skin) of high-speed aircraft increase sharply when the boundary layer changes from laminar to turbulence. This change can increase the difficulty of aircraft design. As known, in hypersonic aircraft, the recovery temperature increases dramatically. Thus it is necessary to cool the wall to protect the aircraft and so an isothermal cold wall condition must be employed. Therefore, there is a realized factor in terms of industrial application in investigating wall temperature effects of hypersonic compressible turbulent boundary layers. Most regions of the flow around a hypersonic aircraft can be modeled as a flat-plate turbulent boundary layer. As a result, the investi-

gation of such turbulence has extensive representative possibilities.

Recently, most direct numerical simulations (DNS) of compressible turbulence have focused on the compressibility effects, particularly to verify the range of the Mach number for the validity of Morkovin's hypothesis [1]. This hypothesis indicates that, at a moderate freestream Mach number ($Ma_\infty \leqslant 5$), the dilatation is small, and any differences from incompressible turbulence can be considered by the mean variations in the fluid properties. Hitherto, this scenario is the basis for the analysis of compressible turbulence.

Rai et al. [2] investigated the boundary conditions and the DNS of the compressible turbulent boundary layer with Ma_∞=2.25 and $Re_\theta \approx 6000$. Furthermore, the DNS results of the spatial simulations are studied for the compressible boundary layer with Ma_∞=2.25 and Re_∞=635000 over the flat-plate boundary layer [3–5]. The results show that the essential dynamics of the turbulent boundary layer closely

resemble the incompressible case. Pirozzli and Bernardini [6] proposed the meticulous structure of a spatially evolving supersonic boundary layer by DNS with Ma_∞=2 up to Re_τ=1120. Such a result allows us to start probing the effects of high Reynolds numbers. Maeder et al. [7] investigated the effects of the Mach number and the wall temperature by using temporal simulations for the compressible boundary layer with Ma_∞=3, 4.5, 6 and a constant wall temperature T_w/T_∞=2.5, 4.4, 7 and $Re_\theta\approx3000$ over a flat-plate boundary layer. The results demonstrate that Morkovin's hypothesis and the strong Reynolds analogy (SRA) are still valid for $Ma_\infty\lesssim6$ for a different wall temperature. Recently, Martin [8] and Duan et al. [9–11] proposed a series of investigations on the compressible turbulence boundary layer over a flat-plate by the temporal evolving DNS, to assess the effects of wall temperature, Mach number and high enthalpy on the Morkovin's hypothesis and SRA. In general, when Ma_∞=5, Morkovin's hypothesis is still considered valid for different wall temperatures. The compressibility effects can be enhanced when decreasing the wall temperature, but they remain insignificant. Moreover, when the wall temperature approximates the recovery temperature, a similar conclusion can be seen for freestream Mach number changes from 0.3 to 12. Lagha et al. [12,13] also studied the effects of the Mach number on turbulent statistics and the near-wall turbulent structure with wall temperature near to recovery temperature by temporal evolution method.

However, the DNS of spatially evolving turbulent boundary layer flow use very large computational effort and memory. Furthermore, those requirements increase rapidly with increase of Mach number and Reynolds number in order to satisfy the demands of DNS.

Liang et al. [14] proposed the DNS results of the spatially evolving boundary layer at Mach 8 over the flat-plate boundary with T_w/T_∞=10.03, which closes to 80% recovery temperature. The result shows that the compressibility effects is weak, and Morkovin's hypothesis remained, thus SRA is still considered valid. On the contrary, this report presents the DNS results for the cold wall case (T_w/T_∞=1.9) for Ma_∞=8 and assesses the wall temperature effects on Morkovin's hypothesis and SRA.

2   Numerical methods and simulation parameters

In the present paper, the subscript "*w*" denotes the wall condition, "∞" denotes freestream and "δ" denotes the outer edge of the boundary layer. Superscript "*" denotes the dimensional flow variable. Also, the dimensionless flow variables are denoted by the same dimensional notation, but without the superscript "*".

Non-dimensionalisation for the NS equations is conducted through flow velocities by utilizing freestream ve-

locity, u_∞^*, length scales of an inch, l_∞^*, density, ρ_∞^*, pressure, $\rho_\infty^*(u_\infty^*)^2$, temperature, T_∞^*, viscosity coefficient μ_∞^* and time, l_∞^*/u_∞^*.

The convection terms in NS equations are approximated by the 7th-order WENO scheme, the viscous terms are approximated by using the 8th-order central difference scheme [15], and the third-TVD type Runge-Kutta method is used for advancing time.

The Cartesian coordinate system is employed, the *x* axis being the streamwise direction, the *y* axis being the normal-to-wall direction and the *z* axis being the spanwise direction. Figure 1 shows a demonstration of the grid in the *xoy* plane. In order to capture the rapid change in the flow of the boundary layer, an exponential grid distribution is adopted along the wall-normal direction. The details of mesh parameters can be found in Table 1.

Furthermore, the present computation is called case M8T1, and the case of ref. [14] is called M8T2 in the present paper.

To study the heat-transfer effects on compressibility, we perform the DNS of a spatially evolving turbulent boundary layer with a nominal freestream Mach number Ma_∞=8 and a freestream temperature T_∞=169.44 K and T_w/T_∞=1.9 for M8T1 (and 10.03 for M8T2 [14]). The other specific flow conditions are listed in Table 2, where δ is the thickness of the boundary layer (defined as the location where the flow velocity is 99% of the free stream velocity) and θ is the momentum thickness. Ma_δ denotes the Mach number at the wedge of boundary layer. Table 2 also provides the different definitions of Reynolds numbers, where $Re_\infty=\rho_\infty u_\infty l_\infty/\mu_\infty$ is the free stream Reynolds number; $Re_\theta=\rho_\delta u_\delta\theta/\mu_\delta$ is the Reynolds number based on the momentum thickness, and the velocity and density at the wedge of the boundary layer; $Re_\tau=\rho_w u_\tau\delta/\mu_w$ is the Reynolds number based on the boundary layer thickness and the wall friction velocity $u_\tau=\sqrt{\tau_w/\overline{\rho}_w}$. Moreover, $Re_{\tau2}=\rho_\delta u_\delta\theta/\mu_w$ which was proposed in ref. [16] is defined by the ratio of the highest momentum ($=\rho_\delta u_\delta^2$) to the wall shear stress ($=\tau_w$) equals to 1.46×10⁴ and 2.01×10⁴ for M8T1 and M8T2, respectively.
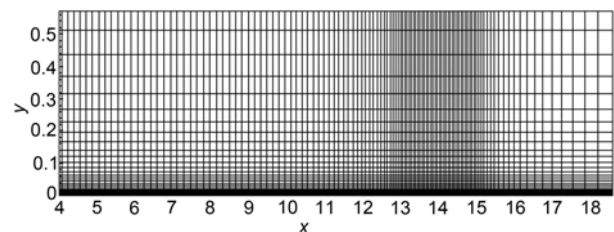

Figure 1   Sketch of the 2D computational meshes in the *xoy* plane.

Table 1   Basic grid mesh parameters for the DNS

Case	$L_x \times L_y \times L_z$	$N_x \times N_y \times N_z$	$\Delta x^+ \times \Delta y^+ \times \Delta z^+$
M8T1	11×0.7×0.18	8950×90×640	11.2×1.0×4.5
M8T2	37×0.7×0.3	12460×100×320	12.2×0.96×4.6

Table 2   Computational flow parameters

Case	T_w/T_∞	Ma_δ	Re_∞	Re_θ	Re_τ
M8T1	1.9	7.29	2×10⁶	2.2×10⁴	2360
M8T2	10.03	6.92	5×10⁶	7.8×10⁴	1250

3   Turbulence statistics

In present paper, $\overline{f}$ denotes the Reynolds average of *f*, and $\tilde{f} = \overline{\rho f} / \overline{\rho}$ denotes the Favre average of *f*. Consequently, there are two types of fluctuating variables, $f' = f - \overline{f}$ and $f'' = f - \tilde{f}$.
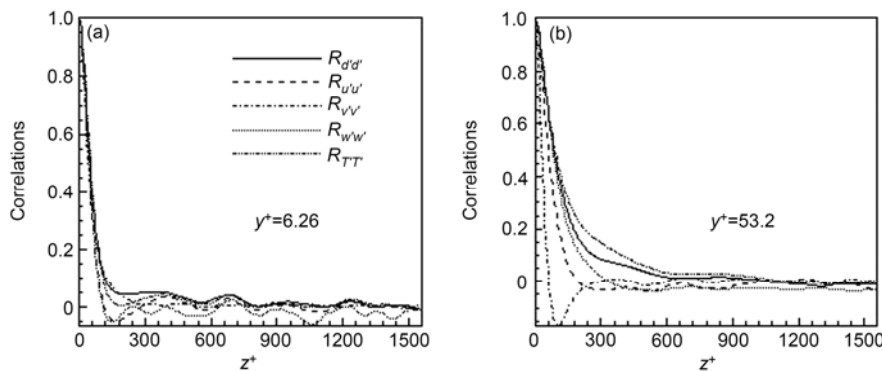
3.1   Two-point correlations

To verify the adequacy of the computational domain size and the grid resolution in the spanwise direction, two-point correlations for the variables density, velocity and temperature are analyzed in the spanwise direction. The correlation coefficient used here is defined as

$$R_{\alpha'\beta'}(y,z) = \frac{\overline{\alpha'(x,y,z'+z)\beta'(x,y,z')}}{\sqrt{\overline{\alpha'(x,y,z')^2}}\sqrt{\overline{\beta'(x,y,z')^2}}}, \tag{1}$$

where overline denotes the average in the spanwise direction and time. Thus, the two-point correlation, $R_{\alpha'\beta'}$, is a function of the spanwise distance of two points at a given position along the normal-to-wall direction. Furthermore, the autocorrelation coefficient can be defined as

$$R_{\alpha'\alpha'}(y,z) = \frac{\overline{\alpha'(x,y,z'+z)\alpha'(x,y,z')}}{\overline{\alpha'(x,y,z')^2}}, \tag{2}$$

is one of methods to verify whether computational region is sufficiently large in the spanwise direction. Figure 2 show

the autocorrelation coefficients of ρ, *u*, *v*, *w*, *T* at *x*=14.5. The autocorrelations decay toward zero near the middle part of the spanwise direction at different wall normal locations. This scenario indicates that the two-point correlations are sufficiently small over a distance of $L_z/2$. Thus, the present computational domain in the spanwise direction is sufficiently wide for the present turbulence-free motion and for DNS.

3.2   Mean skin friction coefficient

Figure 3 depicts the skin friction coefficient, $C_f = \tau_w / (\rho \overline{u}^2 / 2)$, as a function of *x*. $\tau_w = [\overline{\mu} \partial \overline{u} / \partial y]_w$ denotes the wall viscous stress. Moreover, the theoretical estimates of C_f for the fully turbulent regime given by White [17] are also included in Figure 3 and can be written as

$$C_f = \frac{0.455}{S} \left[\ln \left(\frac{0.06}{S} Re_x \frac{1}{\overline{\mu}_w} \sqrt{\frac{1}{\overline{T}_w}} \right) \right]^{-2}, \tag{3}$$

where $S = \frac{1}{\sin^{-1} A} \sqrt{\overline{T}_w - 1}$ and $A = r \frac{\gamma-1}{2} Ma_\infty^2 \frac{1}{\overline{T}_w}$. $\overline{\mu}$ and $\overline{T}_w$ are the average viscosity coefficient and the temperature on the wall, respectively, *r* is the correction coefficient, and *x* is the distance from the edge of the flat-plate boundary. In the present computation, we use $r = 0.0313$. The simulation shows good agreement with the results predicted by eq. (3) in the fully turbulent region. Thus, the present simulation is reliable and valid.

Figure 3 shows that there are three segments that can be divided from the starting point of the transition for the case of M8T1. The first segment, termed the transition region, approximately covers the interval (6.5, 9). Thus, the transition peak lies at $x \approx 9$. The second segment, starting from the transition peak, approximately covers the range (9, 13), where the average slope of the friction coefficient (shown as the dashed dot line in Figure 3) decreases dramatically. In the last segment, the flow further evolves into a fully developed turbulence at about *x*>13. Thus all of present statistics data are taken from this region.

Figure 2   Distribution of the two-point autocorrelations along the spanwise direction at (a) y^+=6.26 and (b) y^+=53.2.

3.3   Mean velocity profile

Figure 4 plots the profiles of DNS and van Direst transformed mean velocity. It indicates some new characteristics of the mean velocity profile for Mach 8 with an extreme cold wall temperature. The region that belongs to the viscous sub-layer decreases to $y^+ \leqslant 2$. The buffer layer and the log-law region approximately cover (2, 90) and (90, 350), respectively. It indicates that the buffer layer enlarges in great extent and the log-law region moves toward outer of boundary layer. However, the Karman constant is held at 0.41. This scenario is differs from the incompressible case. Figure 4 also shows the result [14] which indicates that the profile is similar to that of incompressible. The intervals of viscous sub-layer, buffer layer and log-law regions are approximately [1,5], [5,30] and [30,200] for M8T2, respectively.
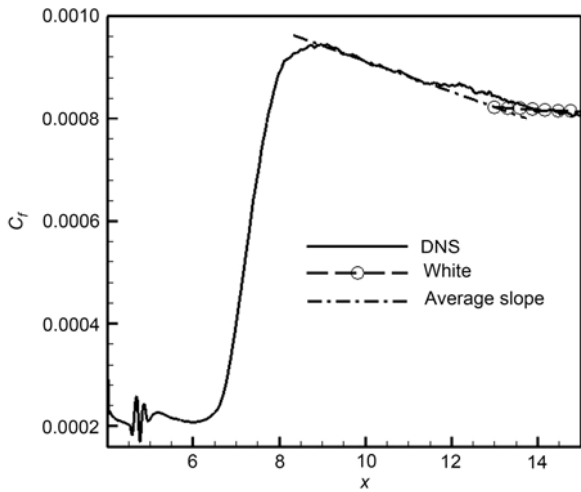

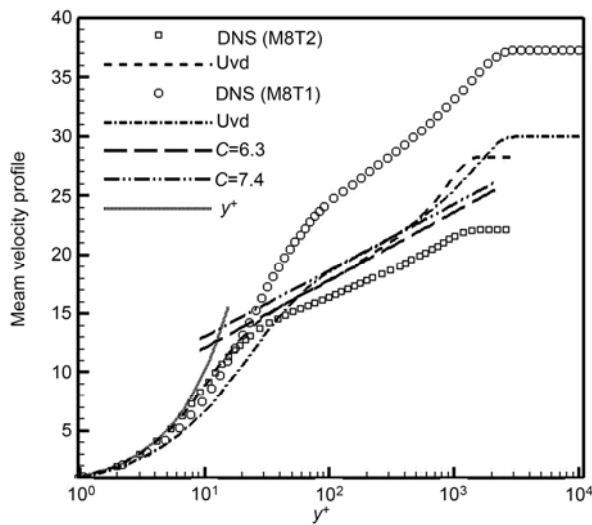**Figure 3**   Distribution of the skin friction coefficient.

Figure 4   Distribution of the mean streamwise velocity.

3.4   Turbulent intensity

Figure 5 plots the turbulent intensity that is normalized by the local streamwise mean velocity component $\bar{u}$ (or denoted as $\langle u \rangle$) for fully developed turbulence. In this paper, the RMS (root-mean-square) of the velocity fluctuation, which is defined as $u'_{rms} = \sqrt{\overline{u'^2}}$ (similar to v'_{rms} and w'_{rms}), is used to measure the intensity of the turbulence. The experimental results for the corresponding incompressible flat-plate boundary layer are denoted by symbols. When the results are plotted versus y^+, Figure 5 shows that there are distinct differences between the present results and the experimental ones, particularly for the RMS of the streamwise velocity fluctuations.

However, the present investigation shows that the above results are not always compatible, which is primarily caused by an improper wall scale y^+ (called traditional non-dimension wall scale). Huang et al. [18] have proposed new wall coordinates, y^*(called a semi-local non-dimension wall scale). They are defined as

$$y^+ = \frac{y}{l^+}, \; l^+ = \frac{\mu_w}{\rho_w u_\tau}, \; u_\tau = \sqrt{\frac{\tau_w}{\rho_w}}, \qquad (4)$$

$$y^* = \frac{y}{l^*}, \; l^* = \frac{\bar{\mu}(y)}{\bar{\rho}(y)u_\tau^*}, \; u_\tau^* = \sqrt{\frac{\tau_w}{\bar{\rho}(y)}}, \qquad (5)$$

where τ_w is the wall shear stress. This scenario seems to indicates that y^* is based not only on the wall properties but also on the local mean properties, meanwhile, y^+ is based only on the wall properties. More can be found elsewhere [14].

Moreover, when heat environment changes in flat-plate boundary layer, eq. (5) will change consequently. For hypersonic flow case, such changes are considered more serious. Although Huang et al. [18] draw the conclusion that y^*
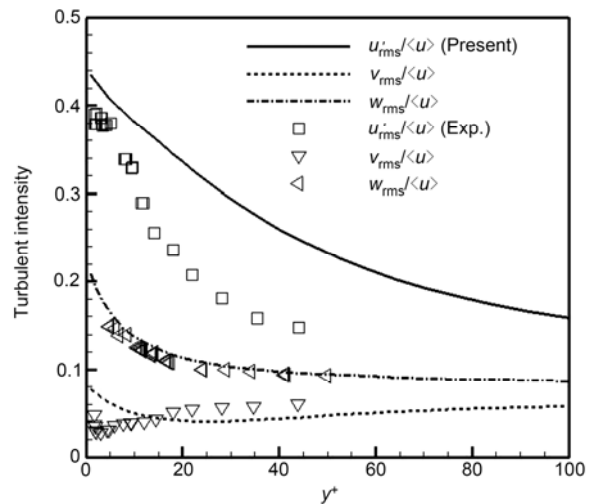

Figure 5   Turbulence intensity vs. y^+ for M8T1 and experiment.

is perhaps better than y^+, they did not conduct a high Mach number flow investigation. Moreover, these two wall coordinators are almost identical for incompressible flow case because of density and temperature almost are constants through the boundary layer.

Figure 6 shows the turbulent intensity versus y^*. It clearly shows that all of the DNS results are in good agreement with the experimental results. Liang et al. [14] have proposed similar results for the case M8T2. Thus, the turbulent intensities are similar for different wall temperatures. Furthermore, there are notable differences in the DNS results of v'_{rms}, which are independent of the wall coordinate in near wall region. One reasonable explanation, as pointed in ref. [19], is that the strong wall cooling can be seen as a perturbation source or sink that projects or absorbs the energy and impacts the perturbation of the velocity component that is normal to the wall. These will lead to large flow flux, such as heat flux.

The DNS results indicate that, for a high Mach number with an extremely cold wall, y^* is also much better than y^+. When y^* is adopted, the some characteristics of the boundary layer have similarity with the incompressible case.

3.5 Walz equation

One of the commonly used temperature velocity relations for a zero-pressure gradient around the flow of the flat plate is the Walz equation:

$$\frac{\tilde{T}}{\tilde{T}_\delta} = \frac{\tilde{T}_w}{\tilde{T}_\delta} + \frac{\tilde{T}_r - \tilde{T}_w}{\tilde{T}_\delta}\frac{\tilde{u}}{\tilde{u}_\delta} - r\frac{\gamma-1}{2}M_\delta^2\left(\frac{\tilde{u}}{\tilde{u}_\delta}\right)^2, \quad (6)$$

where r is the recovery factor and T_r is the recovery temperature. The recovery factor r is calculated by the following equation:

$$\frac{T_r}{T_\delta} = 1 + r\frac{\gamma-1}{2}M_\delta^2.$$

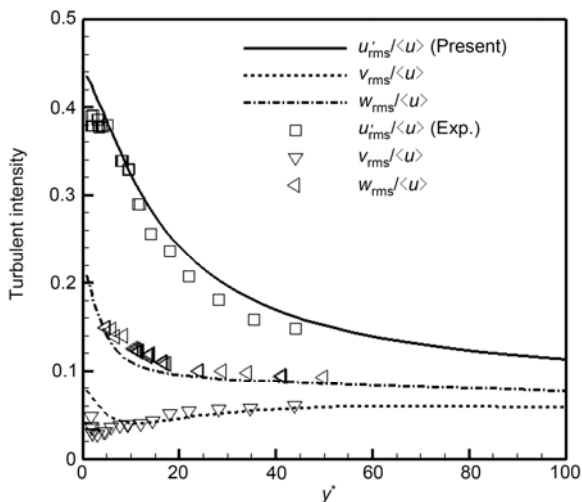Generally $r \approx 0.9$ is used for turbulent boundary layer. It should be noted that the velocity profile in eq. (6) is based on the DNS results. Figure 7 shows the comparison between the results predicted by Walz equation and DNS. The DNS result agrees well with that predicted by eq. (6) for M8T2. This result is consistent with the results proposed by Duan et al. [9], who investigated the effects of the wall temperature at Mach 5 under an isothermal wall with T_w approximating to T_r (or $T_w/T_r \approx 5.4$). For an extremely cold wall, the present case, the maximum mismatch between eq. (6) and the deviation of the DNS results is approximately 10%.

Thus, cooling the wall influences the heat transfer characteristics along wall normal direction in the boundary layer. Such changes lead to some discrepancies of temperature-velocity relation between weak and strong compressible flow. Thus the present difference between results of eq. (6) and DNS is caused by modeling error. Duan and Martin [11] have proposed a improved formula based on Walz equation, which provide better temperature-velocity relation.

4 Reynolds analogies

It is also of importance to consider the statistical average characteristics of the fluctuations in the density and temperature of the compressible boundary layer. Specifically for the case of a high Mach number, the gradient of the temperature is high, which directly impacts the relations between the velocity fluctuation and temperature fluctuation as well as those between heat transfer and skin friction on the wall. These relations can be described by a Reynolds analogy. Walz equation and Reynolds analogy are called temperature velocity relations which can be used to instead of energy (or temperature) equation in engineering application. Morkovin [1] proposed strong Reynolds analogy (SRA) relations, four of which are listed below:
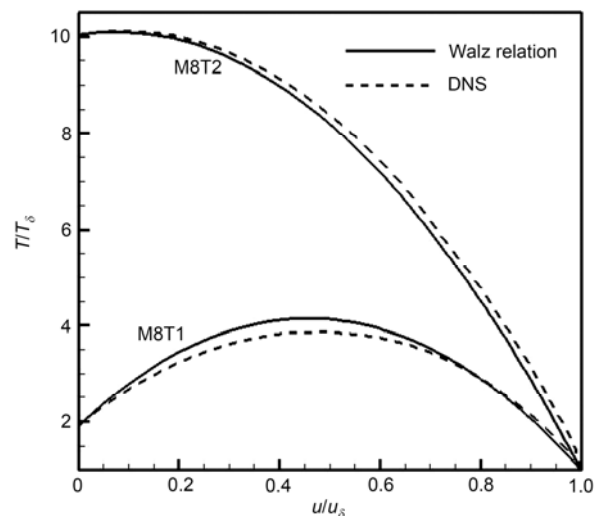

Figure 6 Turbulence intensity versus y^* for M8T1 and experiment.

Figure 7 Test of Walz eq. (6) for different wall temperatures.

$$\frac{T''_{\mathrm{rms}} / \tilde{T}}{(\gamma - 1)Ma^2(u''_{\mathrm{rms}} / \tilde{u})} \approx 1, \qquad (7)$$

$$R_{u''T''} \approx -1, \qquad (8)$$

$$R_{u''v''} = -R_{v''T''}\left[1 - \frac{\overline{v''T''_t}}{\overline{v''T''}}\right], \qquad (9)$$

$$Pr_t = \frac{\overline{\rho u''v''}(\partial \tilde{T} / \partial y)}{\overline{\rho v''T''}(\partial \tilde{u} / \partial y)} \approx 1, \qquad (10)$$

where $Ma^2 = \tilde{u}^2 / (\gamma R \tilde{T})$ is the local Mach number. Pr_t is called the turbulent Prandtl number and is a measure of the ratio of the turbulent kinematic heat transfer over the turbulent kinematic moment transfer.

In further developments that are based on considering the influence of the heat flux on the wall or eliminating the influence of the wall temperature, modified SRA relations have been proposed. For example, Cebeci and Smith [20] derived an extended SRA (ESRA) based on eq. (7):

$$\frac{T''_{\mathrm{rms}} / \tilde{T}}{(\gamma - 1)Ma^2(u''_{\mathrm{rms}} / \tilde{u})} \approx \left[1 + C_p\frac{\tilde{T}_w - \tilde{T}_{t\delta}}{\tilde{u}\tilde{u}_\delta}\right], \qquad (11)$$

where T_t denotes the total temperature. The SRA and ESRA values agree well with experiments for boundary layers with adiabatic walls. However, Gaviglio [21] noted out that SRA and ESRA are not adequate for isothermal wall flows. This point has been verified by the present study. Gaviglio [21], Rubesin [22] and Huang et al. [18] also have proposed modified SRA relations, denoted as GSRA, RSRA and HSRA, which correspond to $c=1.0$, $c=1.34$ and $c=Pr_t$, respectively, in the following equation:

$$\frac{T''_{\mathrm{rms}} / \tilde{T}}{(\gamma - 1)Ma^2(u''_{\mathrm{rms}} / \tilde{u})} \approx \frac{1}{c[1 - \partial \tilde{T}_t / \partial \tilde{T}]}. \qquad (12)$$

Eqs. (7), (11) and (12) indicate ratios near to 1 if Morkovin's hypothesis is valid. Figure 8 shows the SRA and the modified SRA. It shows that if the wall temperature is low, then the SRA equals to about 0.3, which is far less than 1 for the present case. The value of ESRA nears to 1 when about $y^+>80$. However, when the values of the HSRA and GSRA near 1 in which $y^+>200$, still far from the wall. The prediction of the RSRA is far larger than 1. Thus it can be concluded that the classical SRA is no longer valid and the ESRA can better predict results than other modified SRA in strong cold wall cases.

Eq. (8) indicates that u'' and T'' have a negative correlation. As shown in Figure 9, the wall temperature impacts the distribution of the above correlations negatively in the near-wall region, and such dependent relations quickly degrade in the largest region that is far away from the wall. In the present investigation, it is shown that u'' and T'' are not completely negative in correlation. Positive correlation is found at $y^+<40$. $R_{u''T''}$ is approximately -0.6 through most of the boundary layer for $y^+>100$, and similar results have been reported [7,9,21].

Additionally, eq. (9) implies that $R_{u''v''}$ and $R_{v''T''}$ are strongly contrary according to the classical SRA. Figure 9 also shows that $R_{v''T''}$ is approximately 0.4 and $R_{u''v''}$ is near to -0.4 when far away from the wall (about for $y^+>50$). Such results not only test the contrary nature of $R_{u''v''}$ and $R_{v''T''}$, but also indicate that the correlation of u'' and v'' is not considered strong, as well as weak correlation between v'' and T''. Such results are similar [3] for the lower Mach number case. When $y^+<50$, the predicted results by eqs. (8) and (9) are not consistent.

Similar to the definition of Pr_t as in eq. (10), the Prandtl number for turbulent mass diffusion, Pr_ρ, is defined as
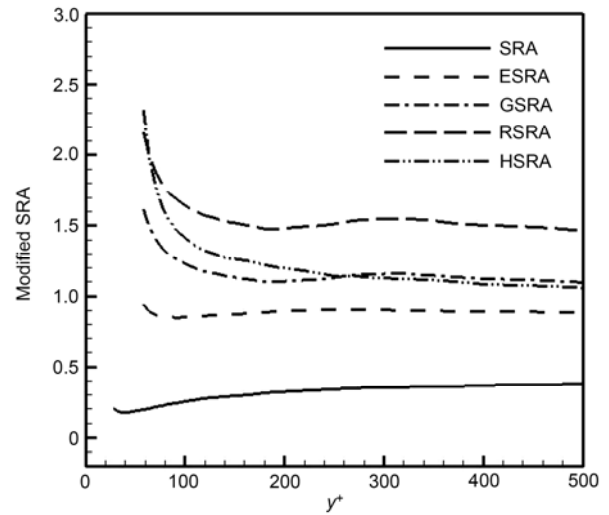
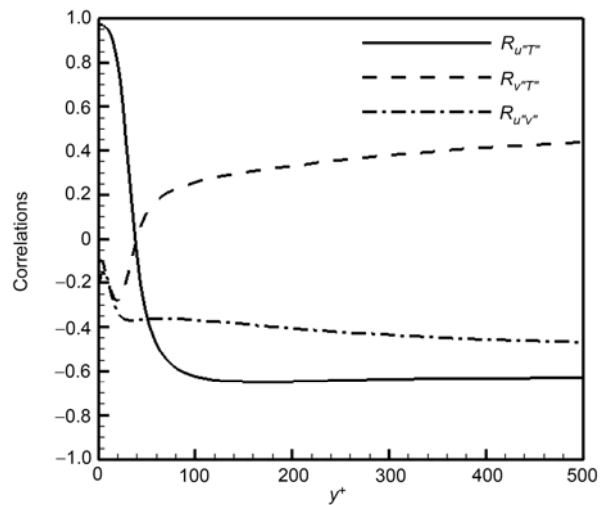**Figure 8**   Distribution of SRA and modified SRAs vs. y^+.

Figure 9   Distribution of $R_{u''T''}$, $R_{v''T''}$ and $R_{u''v''}$ vs. y^+.

$$Pr_\rho = \frac{\overline{u''v''}(\partial \overline{\rho}/\partial y)}{\overline{\rho v''}(\partial \tilde{u}/\partial y)}. \qquad (13)$$

Pr_ρ is a measure of the ratio of the turbulent kinematic viscosity over the turbulent mass diffusivity. Morkovin's hypothesis also implies that Pr_t and Pr_ρ approximates 1 [3]. Figure 10 depicts the distributions of the turbulent Prandtl numbers for the case of M8T1. It is shown that cooling the wall has considerable impacts on Pr_t and Pr_ρ. Both are far from 1 for $y^+<160$. When $y^+>160$, which lies in the log-law region to the outer edge of the boundary layer, $Pr_t \approx Pr_\rho$ with the order of 1.

However, Liang et al. [14] proposed that the SRA is valid for $T_w/T_\infty=10.03$ and $Ma_\infty=8$ in whole boundary layer. Similar results have been reported for Mach 2.25 [3] and 5 [9].

5　Turbulent kinetic energy budget

The turbulent kinetic energy (TKE) is defined as $K = \frac{1}{2}\overline{\rho u''_j u''_j}/\overline{\rho}$, and the compressible turbulent kinetic energy equation reads

$$\frac{\partial}{\partial t}(\overline{\rho}K) = -C + P + T + \prod + D + M + \varepsilon, \qquad (14)$$

where $C = \partial(\tilde{u}_j \overline{\rho}K)/\partial x_j$ is the convection term; $P = -\overline{\rho u''_j u''_i}\partial \tilde{u}_i/\partial x_j$ is the production term caused by the mean velocity gradient; $T = -\partial(\frac{1}{2}\overline{\rho u''_i u''_i u''_j})/\partial x_j$ is the turbulent transport; $\Pi = -\overline{u''_j \partial p/\partial x_j}$ is the pressure term that can be divided into the pressure transport term ($\Pi_t = -\partial(\overline{p'u''_j})/\partial x_j$) and the pressure dilatation term ($\Pi_d = \overline{p'\partial u''_i/\partial x_i}$);

$D = \partial(\overline{u''_i \sigma''_{ij}})/\partial x_i$ is the viscous diffusion term; $M = M_0 + \Pi_p$ is density fluctuations term that accounts for the sum of the mean flow viscous stress diffusion term ($M_0 = \overline{u''_i}\partial \overline{\sigma}_{ij}/\partial x_j$) and the pressure work done term ($\Pi_p = -\overline{u''_j}\partial \overline{p}/\partial x_j$); and $\varepsilon = \overline{\sigma'_{i,j}\partial u''_i/\partial x_j}$ is the molecular viscous dissipation term that accounts for the sum of the solenoidal dissipation part ($\varepsilon_s = -\overline{\mu\omega''_i\omega''_i}$), the dilatational dissipation part ($\varepsilon_d = -\frac{4}{3}\overline{\mu(\partial u''_i/\partial x_i)(\partial u''_k/\partial x_k)}$) and the contribution from inhomogeneous effects part ($\varepsilon_i = \varepsilon - \varepsilon_d - \varepsilon_s$).

Figure 11 plots the turbulence kinetic energy budget versus y^+. All of the terms are normalized by the viscous dissipation term at the wall, that is, ε_w. It was clearly found that the turbulent kinetic energy production term P, the transport term T, the viscous diffusion term D and the viscous dissipation term ε are dominant, and the other terms are incremental. However, the position of maximum value of P is about $y^+ \approx 30$, which is larger than the classical value of about $y^+ \approx 12$ [9,12,14]. If we plot the turbulent kinetic budget terms versus the semi-local wall coordinate y^+, as shown in Figure 12, the profiles collapsed more consistently to the traditional case.

To compare the wall temperature effects on the turbulent kinetic transport, the dominative terms, P, T, D, ε, normalized by the wall viscous dissipation ε_w, are plotted in Figure 13 for case M8T1 and M8T2. As shown in Figure 13, when the these terms are plotted versus y^*, there exists only a small difference in the position of the extreme value between two cases. Furthermore, the position of peak value of P is at about $y^* \approx 12$. The results [3,5,9,12,14] are taken from the adiabatic or near to recovery temperature wall case, which does not cause significant compressibility. Thus, we believe that the present difference is caused by compressi-
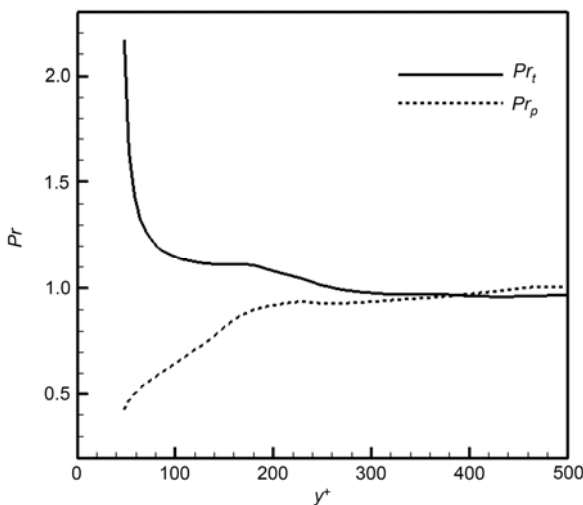

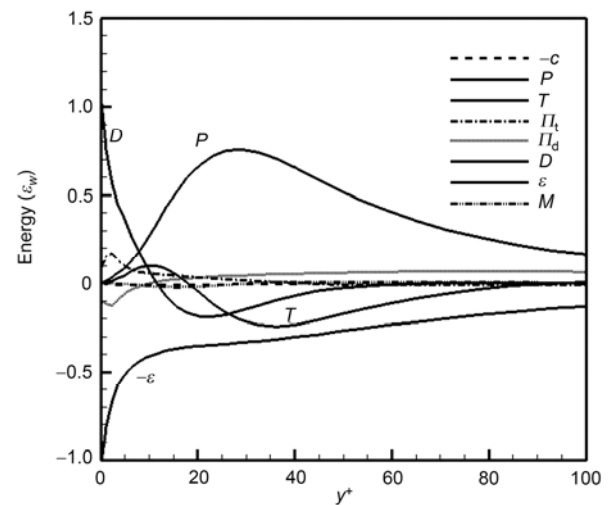**Figure 10**　Distribution of Pr_t and Pr_ρ vs. y$^+$.

Figure 11　Turbulent kinetic energy budget vs. y$^+$.

bility effects. The most active region of TKE lies in buffer layer. Another reason is that, as shown in Figure 4, the multi-layer structure (describe by y^+) depends severely on the wall temperature.

Changing the wall temperature will influence the distribution of the temperature in the boundary layer and will further to impact the turbulent motion. Typically, increasing the wall temperature can enhance the movements of the terms P, T, D, ε. An increase in the wall temperature is helpful for producing turbulent kinetic energy, as shown in Figure 13, with a maximum value of P equal to 0.7 for cold wall case and 1.4 for heater wall case, respectively. The other terms have similar change law with the wall temperature.

6   Compressibility effects

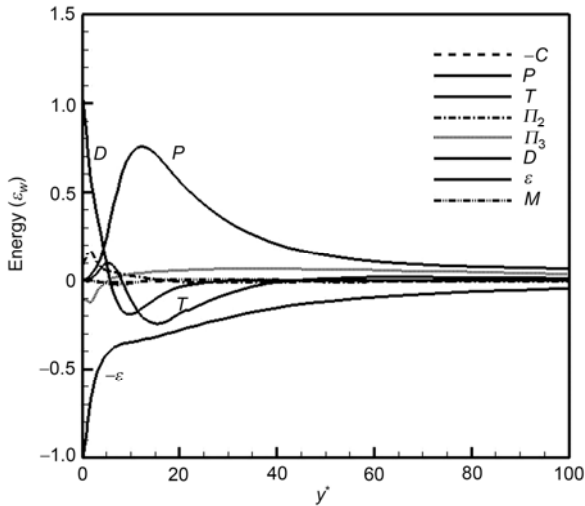In the case of a high Mach number ($Ma_\infty > 5$), in the tradi-

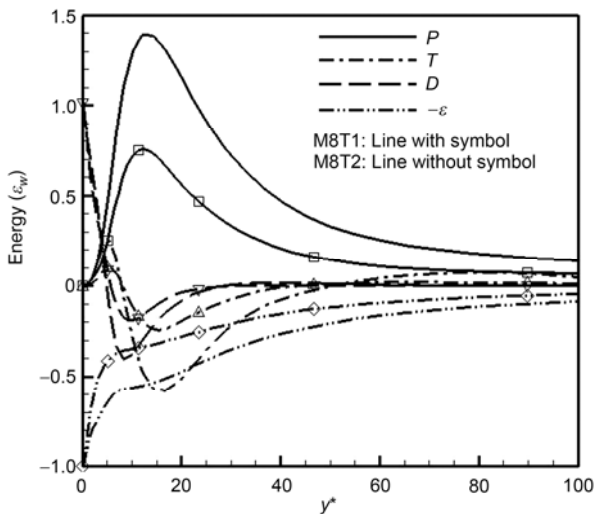**Figure 12**   Turbulent kinetic energy budget vs. y^*.

Figure 13   Comparison of the TKE budget for M8T1 and M8T2.

tional approach, the compressible effects usually strengthen and cannot be neglected. However, the investigation of the compressible flat-plate turbulent boundary layer with $Ma_\infty = 5$ and different wall temperatures in ref. [9] shows that the compressibility effects are weak such that their influence can be omitted. Li et al. [5] studied a similar problem with $Ma_\infty > 6$ and $T_w / T_\infty = 6.98$. The results show that the compressibility effects are also weak. The similar results also can be found for M8T2 [14].

Here, the compressibility effect is also studied by the analysis of the turbulent Mach number (M_t), the probability density function (PDF) of the dilatation term.

6.1   Turbulent Mach number

The turbulent Mach number is defined as

$$M_t = \sqrt{\overline{u'^2 + v'^2 + w'^2}} / \overline{c}, \qquad (15)$$

where $\overline{c}$ is the local sound speed and is one of the important parameters for measuring the compressibility effects. Figure 14 indicates that the turbulent Mach number increases considerably with a decreasing wall temperature in the near-wall region. The peak value of M_t up to 0.59 for the case M8T1 (with a cold wall), and decreases to 0.42 for the case of [5] (with a medium wall temperature), and further decreases to 0.4 for the case M8T2 (with a warmer wall). Moreover, through the whole boundary layer, the turbulent Mach number for the colder wall is far larger than that for the warmer wall. This scenario arises mainly from the local sound speed, $\overline{c} = \sqrt{\gamma R \overline{T}} = \sqrt{\overline{T}} / Ma_\infty$, which depends closely on the local mean temperature. At the same time, the temperature in the near-wall region is severely impacted by the wall temperature. As a result, M_t increases with a decrease in the wall temperature. Similar results have been seen in ref. [9] for $Ma_\infty = 5$ and differing wall temperature.

6.2   PDF of dilatation term

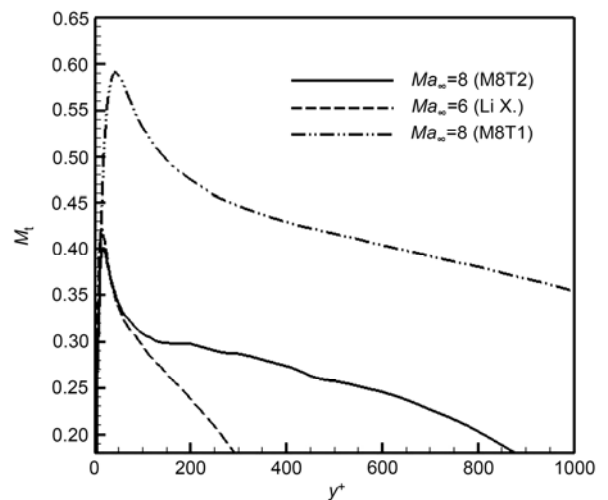The dilatation term $\vartheta = \nabla \cdot V'$ is another critical character-

Figure 14   Turbulent Mach number for different case [5,14].

istic variable that is associated with compressibility effects. It is zero for an incompressible flow or incremental for low freestream Mach number (or a turbulent Mach number is less than 0.3). The PDF of dilatation term can be used to assess probability distribution of compressibility in real space. Figure 15 shows the PDF of ϑ at different normal location to the wall. It indicates that the probability of larger values of $|\vartheta|$ lies in region for $y^+ < 300$. However, the value is less than 0.3% which is insignificant. Moreover, the probabilities of compression and dilatation procedure are almost identical. Generally, the PDF of these two procedure follows the normal distribution. Thus, relative stronger compression procedure concentrates in near-wall region for $y^+ < 300$. In excess of this, the flow almost is incompressible.

It can be found that although the curves in Figure 15 differ, they maintain some similarities. If the PDF of $\overline{\rho}\vartheta$ (or $\langle \rho \rangle \vartheta$) is computed, as shown in Figure 16, the curves collapse well. Similar results have been reported elsewhere [12].

7   Near-wall turbulent structure

Figure 17 shows the distributions of the instantaneous streamwise velocity along the spanwise direction for $x \in$ [13.5, 14.56] at approximately $y^+ \approx 15$. In Figure 17, the coordinate is normalized by the thickness of the boundary layer at x=14.5. Several long regions at a low speed u with deep dark are identified. There are some distinct features for present results. Firstly, the streaks become flatter for M8T1 (a cold wall) than for M8T2 (a warmer wall). According to previous analysis, it is the result of enhancement of a compressibility effect. Secondly, the streaks remains longer for a cold wall (case M8T1) than for a warmer wall (M8T2).
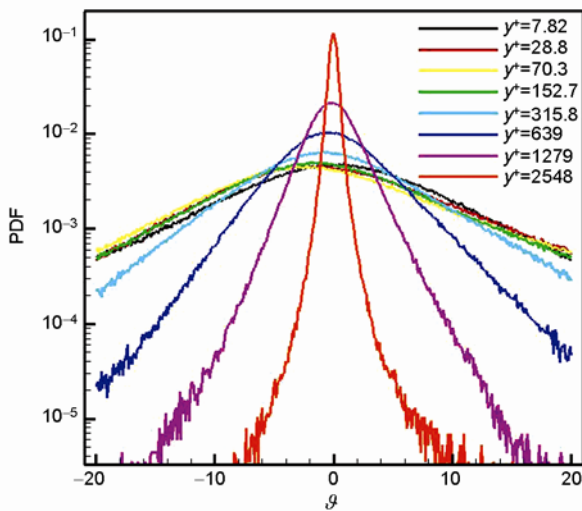
The length of some streaks are approximately 6δ–8δ in the case of M8T1. Thus, reducing the wall temperature increases the streamwise coherency of near-wall streaks. Thirdly, the average spanwise spacing of near-wall streaks is approximately 229 wall units, which is much larger than the traditional value (approximately 100 wall units) for incompressible or weak compressible cases. One reason may be that the length of wall unit depends severely on the wall temperature. The values are about 6×10^{-5} and 2×10^{-4} for M8T1 and M8T2, respectively. Moreover, the changes of streaks do not adjust synchronously.

Figure 18 shows the instantaneous isosurface of Q=600, where Q is the second invariant of the velocity gradient tensor. Figures 18(a) and (b) show Q at the transition region, (7.5, 8), and the fully developed turbulence region, (14, 14.5), respectively. In comparison with M8T2 and other lower Mach number with higher wall temperature cases [5,9,13], it can be seen that the coherence vortices are arranged to be smoother and streamwised, and the hair-pin vortices occasionally occur in the strong cold wall condition. Thus, it is helpful to maintain the vortices structure in the streamwise direction when the wall temperature decreases.

8   Conclusions

The DNS for the spatially evolving hypersonic boundary layer turbulence over a flat plate at Mach 8 with T_w/T_∞=1.9 has been performed by using the 7th-order WENO scheme combined with the 8th-order central scheme. The effects of surface heat transfer on the boundary layer flow are investigated. The compressibility effects and the statistical characteristics of the turbulence also have been analyzed. Some conclusions can be drawn as follows.

Cooling the wall can enhances the compressibility effect. It is sufficiently strong to impact some of the statistical results for present case. It impacts the mean velocity profile.
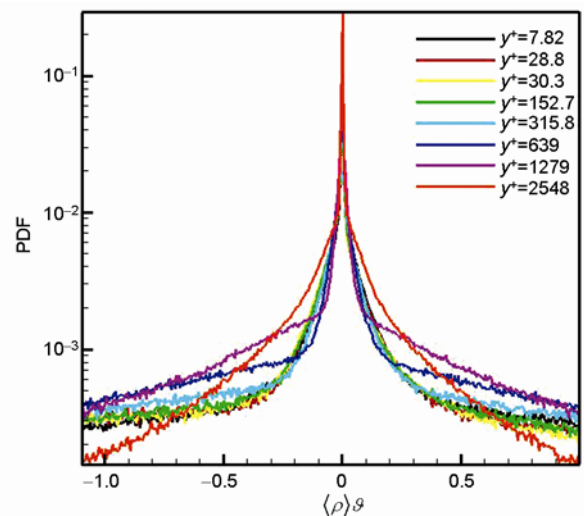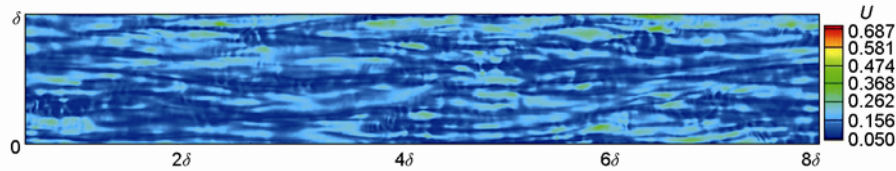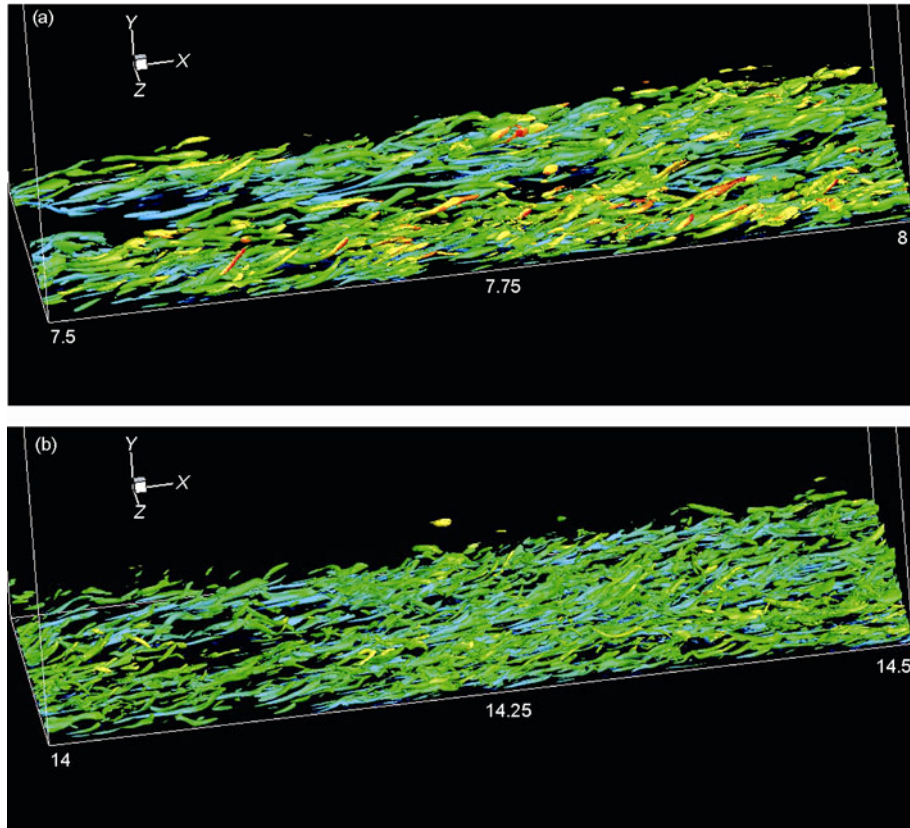

Figure 15   PDF of dilatation term at different wall normal locations.

Figure 16   PDF of dilatation term at different wall normal locations.

Figure 17 Near-wall streak structure at about y^+=15.

Figure 18 Instantaneous isosurface of Q=600 at (a) the transition region, and (b) the fully developed turbulence region.

As a result, the buffer layer enlarges from the traditional interval approximately (5, 30) (the incompressible case) to the present of (2, 90). Moreover, the viscous sub-layer shrinks and log-law layer moves towards to outer edge. With enhancement of the compressibility effect, the coherence vortices are arranged to be smoother and more streamwise, with the hair-pin vortices occasionally occurring in the strong cold wall condition. The steaks are also arranged to be flatter and longer.

The Walz equation is still valid for the present cases. However, the predicted results still have small deviations (less than 10%) as compared to the results of the DNS. This can be attributed to modeling errors.

The strong Reynolds analogy (SRA) depends closely on the wall temperature. The classical SRA is no longer valid and the ESRA can predict results better than other modified SRA in the present case. It is still valid for the case of wall temperature near the recovery temperature.

In TKE budgets, decreasing the wall temperature can constrain the motion of the production term, the transport term, the viscous diffusion term and the viscous dissipation term, which are dominant terms in TKE.

During the investigation of hypersonic wall turbulence, a semi-localized wall coordinate (y^*), is better than the traditional wall coordinate (y^+). Thus, as suggested in an investigation of the channel turbulence at a middle-range Mach number [18], we recommend further use of y^* in the analysis of supersonic and hypersonic wall turbulence.

1   Morkovin M V. Effects of compressibility on turbulent flows. In: Favre A, ed. Macutee Canique de la Turbulence. CNRS, 1962. 367–380

2   Rai M M, Gatski T B, Erlebacher G. Direct simulation of spatially evolving compressible turbulent boundary layers. AIAA Paper, 1995, 1995-0583

3   Pirozzoli S, Grasso F. Direct numerical simulation and analysis of a spatially evolving supersonic turbulent boundary layer at Ma=2.25. Phys Fluids, 2004, 16: 530–545

4   Gatski T B, Erlebacher G. Numerical Simulation of a Spatially Evolving Supersonic Turbulent Boundary Layer. Technical Report 211934, NASA Tech, TM, 2002

5   Li X L, Fu D X, Ma Y W. Direct numerical simulation of a spatially evolving supersonic turbulent. Chin Phys Lett, 2006, 23: 1519–1522

6   Pirozzoli S, Bernardini M. Turbulence in supersonic boundary layers at moderate Reynolds number. J Fluid Mech , 2011, 688: 120–168

7   Maeder T, Adams N A, Kleiser L. Direct simulation of turbulent supersonic boundary layers by an extended temporal approach. J Fluid Mech, 2001, 429: 187–216

8   Martin M P. DNS of hypersonic turbulent boundary layers. AIAA Paper, 2004, 2004-2337

9   Duan L, Beekman I, Martin M P. Direct numerical simulation of hypersonic turbulent boundary layers. Part 2: Effect of wall temperature. J Fluid Mech, 2010, 655: 419–445

10 Duan L, Beekman I, Martin M P. Direct numerical simulation of hypersonic turbulent boundary layers. Part 3: Effect of Mach number. J Fluid Mech, 2011, 672: 245–267

11 Duan L, Martin M P. Direct numerical simulation of hypersonic turbulent boundary layers. Part 4. Effect of high enthalpy. J Fluid Mech, 2011: 684: 25–59

12 Lagha M, Kim J, Eldradge J D, et al. A numerical study of compressible turbulent boundary layers. Phys Fluids, 2011, 23: 015106

13 Lagha M, Kim J, Eldradge J D, et al. Near-wall dynamics of compressible boundary layers. Phys Fluids, 2011, 23: 065109

14 Liang X, Li X L, Fu D X, et al. DNS and analysis of a spatially evolving hypersonic turbulent boundary layer over a flat plate at Mach 8 (in Chinese). Sci Sin-Phys Mech Astron, 2012, 42(3): 282–293

15 Liang X, Li X L, Fu D X, Ma Y W. Complex transition of double-diffusive convection in a rectangular enclosure with height-to-length ratio equal to 4. Part 1. Commun Comput Phys, 2009, 6: 247–268

16 Fernholz H H, Finley P J. A Critical Commentary on Mean Flow Data for Two-dimensional Compressible Boundary Layers. Technical Report, AGARD-AG-253, 1980

17 White F M. Viscous Fluid Flow. New York: McGraw-Hill, 1974. 367–380

18 Huang P G, Coleman G N, Bradshaw P. Compressible turbulent channel flows: DNS results and modeling. J Fluid Mech, 1995, 305: 185–218

19 Mack L M. Linear stability theory and the problem of supersonic boundary-layer transition. AIAA J, 1975, 13: 278–289

20 Cebeci T, Smith A M O. Analysis of turbulent boundary layers. New York: Academic Press, 1974

21 Gaviglio J. Reynolds analogies and experimental study of heat transfer in the supersonic boundary layer. Int J Heat Mass Transfer, 1987, 30(5): 911–926

22 Rubesin M W. Extra compressibility terms for favre-averaged two-equation models of inhomogeneous turbulent flows. Technical Report, 177556, NASA Tech CR, 1990